

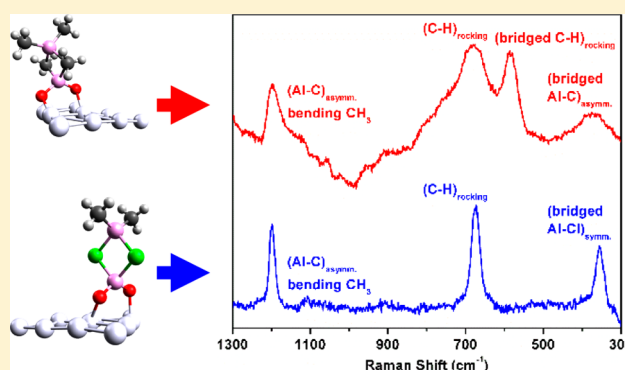
# Identification of Dimeric Methylalumina Surface Species during Atomic Layer Deposition Using *Operando* Surface-Enhanced Raman Spectroscopy

Ryan A. Hackler,<sup>†,‡</sup> Michael O. McAnally,<sup>†</sup> George C. Schatz,<sup>†</sup> Peter C. Stair,<sup>†,‡</sup> and Richard P. Van Duyne<sup>\*,†,‡</sup>

<sup>†</sup>Department of Chemistry and <sup>‡</sup>Center for Catalysis and Surface Science, Northwestern University, Evanston, Illinois 60208, United States

## S Supporting Information

**ABSTRACT:** *Operando* surface-enhanced Raman spectroscopy (SERS) was used to successfully identify hitherto unknown dimeric methylalumina surface species during atomic layer deposition (ALD) on a silver surface. Vibrational modes associated with the bridging moieties of both trimethylaluminum (TMA) and dimethylaluminum chloride (DMACl) surface species were found during ALD. The appropriate monomer vibrational modes were found to be absent as a result of the selective nature of SERS. Density functional theory (DFT) calculations were also performed to locate and identify the expected vibrational modes. An *operando* localized surface plasmon resonance (LSPR) spectrometer was utilized to account for changes in SER signal as a function of the number of ALD cycles. DMACl surface species were unable to be measured after multiple ALD cycles as a result of a loss in SERS enhancement and shift in LSPR. This work highlights how *operando* optical spectroscopy by SERS and LSPR scattering are useful for probing the identity and structure of the surface species involved in ALD and, ultimately, catalytic reactions on these support materials.



## INTRODUCTION

Atomic layer deposition (ALD) is a technique that employs sequential, self-limiting reactions between gaseous precursor molecules and a substrate to deposit thin films and nanoparticles in a controlled manner.<sup>1–4</sup> Films grown via ALD are highly uniform, conformal, and pinhole-free, and can be deposited on most substrates of any morphology, provided there is some type of nucleation site at which the surface chemistry can take place. Nanoparticles grown via ALD can also be grown on a variety of supports, with certain control over size and dispersity. As a result of the simplicity and ease in control, a variety of ALD methods and procedures have been developed over the years to allow for the deposition of numerous materials, ranging from thin films such as metal oxides,<sup>5,6</sup> metal nitrides,<sup>7</sup> metal sulfides,<sup>8</sup> and pure metal films,<sup>9</sup> to metal nanoparticles such as Pd,<sup>10–13</sup> Pt,<sup>14–16</sup> and Ag,<sup>17</sup> among others.<sup>18–21</sup> These ALD-grown materials have experienced increasing attention and have found applications in catalysis,<sup>22</sup> microelectronics,<sup>23</sup> and most recently MOF metalation<sup>24</sup> and biomimetic materials.<sup>25,26</sup>

The nucleation and growth rate of any ALD material is dependent on the surface chemistry involved, and such an understanding of how the ALD reaction takes place is required for precisely controlling the specific growth rate on a substrate

at any given ALD temperature.<sup>27,28</sup> The surface chemistry involved in each ALD half-cycle is also important when evaluating which substrates are suitable for a given ALD process. Our previous work has shown *operando* surface-enhanced Raman spectroscopy (SERS) to be a valuable method that is capable of measuring vibrational spectra over several cycles in an ALD process, leading to unique structural information about how the thin film grows on different substrates.<sup>29,30</sup> For example, our previous study has shown alumina ALD on silver from 55 to 100 °C to proceed via ligand exchange<sup>29</sup> as opposed to complete thermal ligand dissociation.<sup>31</sup> The evidence for this mechanism comes from the Al–C and Al–CH<sub>3</sub> vibrations seen in the *operando* SER spectra. These vibrations would not show up in the case of complete thermal ligand dissociation. Questions still remain, however, as to the identity of the surface species during the alumina ALD process, and what species are responsible for the observed SERS response. Methods such as infrared reflection–absorption spectroscopy (IRRAS)<sup>32,33</sup> have failed to provide sufficient information about the structure of the surface species during deposition, due to a lack in surface specificity and difficulty in

Received: December 9, 2016

Published: January 30, 2017

probing the lower wavenumber region ( $<1000\text{ cm}^{-1}$ ) where vibrational modes pertinent to the structure are located. SERS, on the other hand, is capable of obtaining such structurally relevant information. We propose that the structure of the methylalumina surface species in question is likely of a dimeric form (containing methyl groups bridging the Al atoms). It is unlikely that the monomer species would yield a measurable SER response in our current setup due to their low Raman scattering cross-section, coupled with the fact that each ALD cycle yields submonolayer coverage of the surface species.

SERS is a highly sensitive vibrational spectroscopic technique<sup>34–36</sup> capable of probing molecules close to a plasmonically active material by exciting the localized surface plasmon resonance (LSPR) of a noble metal nanostructured surface such as Au, Cu, or Ag.<sup>37,38</sup> The electromagnetic excitation results in an amplification of the local electromagnetic field around the metallic nanostructure, leading to greater scattering by nearby molecules. This enhancement process is typically referred to as the electromagnetic (EM) enhancement mechanism<sup>39,40</sup> and is responsible for enhancement factors of up to  $\sim 10^6$ – $10^8$ . The other contribution in overall signal enhancement comes from the chemical enhancement mechanism (CHEM), whereby a molecule directly adsorbed to the metallic surface results in sufficient charge-transfer (in ground or excited states) to change the polarizability derivative. Typically, the CHEM results in  $\sim 10$ – $100\times$  signal enhancements.<sup>41,42</sup>

The work described herein is the most comprehensive *operando* SERS study of surface species during a reaction to date. We used two different alumina precursors, trimethylaluminum (TMA) and dimethylaluminum chloride (DMACl) for the alumina deposition. These two precursors are differentiated by their bridging moieties in the dimer form and symmetry groups in the monomer form, which led to different spectroscopic signatures of the surface species. Comparisons were made between common and unique vibrations between the two precursor depositions to determine the surface species being probed by SERS. Quartz crystal microbalance (QCM) measurements, X-ray photoelectron spectroscopy (XPS), quadrupole mass spectrometry (QMS), *operando* LSPR measurements, and scanning electron microscopy (SEM) were used to quantify the alumina deposition and growth properties for both precursors. Density functional theory (DFT) was used to corroborate potential surface species hypothesized by the experiments.

## EXPERIMENTAL SECTION

**Fabrication of AgFON SERS Substrates.** AgFONs (silver film-over-nanospheres) were fabricated on polished 25 mm silicon wafers according to a standard procedure described in previous publications.<sup>43</sup> Briefly, silicon wafers were cleaned by immersion in piranha solution (3:1 by volume  $\text{H}_2\text{SO}_4/30\%\text{ H}_2\text{O}_2$ ) for 1 h. Clean silicon wafers were thoroughly rinsed with deionized (DI) water. The wafers were then sonicated for 1 h in 5:1:1 by volume  $\text{H}_2\text{O}/\text{NH}_4\text{OH}/30\%\text{ H}_2\text{O}_2$  followed by rinsing with DI water. 390 nm silica (Bangs Laboratories) nanospheres were diluted to 5% silica by volume. The solvent was replaced twice with Millipore  $\text{H}_2\text{O}$  (Milli-Q,  $18.2\text{ M}\Omega\text{ cm}^{-1}$ ) by a conventional centrifugation/supernatant removal procedure, followed by sonication for 1 h. The solvent-replaced nanosphere solution (10–12  $\mu\text{L}$ ) was drop-coated and distributed homogeneously across the silicon wafer surface. The solvent was then allowed to evaporate in ambient conditions where the drop-coated spheres assembled in a hexagonal close-packed array as verified by SEM measurements. 200 nm Ag films were deposited at a rate of  $2\text{ \AA/s}$

under vacuum ( $6 \times 10^{-6}$  Torr) over the nanospheres using a home-built thermal vapor deposition system. The substrates were spun during deposition while the metal thickness and deposition rate were measured by a 6 MHz gold-plated QCM (Sigma Instruments).

**Surface-Enhanced Raman Spectroscopy and Localized Surface Plasmon Resonance Measurements.** A 532 nm continuous wave (CW) laser (Innovative Photonic Solutions) was used for all SERS experiments, and a quartz tungsten-halogen light source (Thorlabs QTH10) was used for all *operando* LSPR measurements. Laser light and lamp light were directed, using protected silver mirrors, to a 3 mm right-angle prism and then focused using a visible achromatic doublet lens (2.54 cm diameter, 10.16 cm focal length), through a quartz window to a plasmonic substrate placed inside the ALD reactor. The laser spot size radius measured at the sample was  $\sim 124\text{ }\mu\text{m}$  using a scanning knife-edge technique. Raman scattered light (for SERS) and reflected light (for LSPR) was collected in a  $180^\circ$  backscattering geometry and focused onto a 0.3 m imaging spectrograph (Acton SpectraPro 2300i) using a visible achromatic doublet lens (2.54 cm diameter, 10.16 cm focal length). Scattered and reflected light was dispersed (1200 grooves/mm, 500 nm blaze grating for SERS, 150 grooves/mm, 500 nm blaze grating for LSPR) onto a liquid  $\text{N}_2$ -cooled CCD detector (Princeton Instruments, model 7509–0001,  $1340 \times 400$  pixels). SER spectra were collected with 1 mW of laser power ( $P_{\text{aq}}$ ), 10 s of acquisition time ( $t_{\text{aq}}$ ), and 10 accumulations each. Extinction spectra were collected via specular reflectance with a silver mirror used as a spectral reference, with 0.01 s of acquisition time and 1000 accumulations in each spectrum. No background contribution or SERS signal attenuation was observed from the quartz window, as previously established.<sup>29</sup>

**Atomic Layer Deposition.** ALD was performed in a home-built viscous flow reactor that has been described previously<sup>29,30</sup> and shown in Figure S1. SERS substrates were mounted on a movable sample holder, placed inside the ALD chamber under vacuum ( $\sim 0.05$  Torr), and heated to  $\sim 70^\circ\text{C}$  for alumina ALD. The ALD chamber was set to  $200^\circ\text{C}$  during Ag ALD (described in detail elsewhere)<sup>17</sup> for QCM and QMS. SER and extinction spectra were acquired before and after dosing 60 sccm of either TMA (Sigma-Aldrich, 97%) or DMACl (Sigma-Aldrich, 97%), and 60 sccm deionized water using ultrahigh purity (UHP)  $\text{N}_2$  as the carrier gas. The timing sequence for alumina ALD was 60s-60s-60s-60s, with SERS measurements collected in-between half-cycles. For Ag ALD, 50 sccm of trimethylphosphine-(hexafluoroacetylacetonato) silver(I) ((hfac)Ag(PMe<sub>3</sub>), Strem Chemicals, 99%) and 60 sccm formalin was used, both using UHP  $\text{N}_2$  as the carrier gas. The (hfac)Ag(PMe<sub>3</sub>) bubbler was heated to  $65^\circ\text{C}$ , and the precursor inlet line was heated to  $100^\circ\text{C}$ .

**In Situ QCM and QMS Measurements.** In situ QCM (Inficon Q-POD + 6 MHz Colorado Crystal Corp.) and QMS (RGA300 Stanford Research Systems) was used to measure  $\text{Al}_2\text{O}_3$  ALD growth rate and reaction products evolved on a silver surface, respectively. To simulate the silver surface of the AgFON substrates used in SERS measurements, 200 ALD cycles of Ag were performed on to the QCM sensor and ALD chamber prior to alumina ALD (done previously for other metal surfaces<sup>31</sup>), with a timing sequence of 60s-60s-60s-60s. Alumina ALD was then performed during QCM and QMS measurements in the same manner as the SERS experiments (with a timing sequence of 60s-60s-60s-60s for QCM and 30s-60s-30s-60s for QMS). The QCM was fitted with a nitrogen purge on the backside to prevent backside deposition. The inlet line to the QMS was heated to  $100^\circ\text{C}$  to prevent condensation. The first introduction of the alumina precursors into the chamber during QMS measurements was ignored for methane measurements, as leftover precursor would decompose in the precursor lines into extra methane from previous experiments and thus not represent methane from ALD. Background signal resulting from the fragmentation of alumina precursor was also subtracted from each dose for the methane ( $m/z = 16$ ) signal. To acquire the background signal, three half-cycles of either TMA or DMACl was done in succession after an initial surface saturation dose to acquire the background signal. The signal from each half-cycle was then averaged and subtracted from each appropriate precursor dose in the data (see Figure S2). No background signal from water fragmentation was

observed during water doses. Acquisition times for all QMS measurements was 1 s unless otherwise specified.

**Scanning Electron Microscopy.** Scanning electron microscopy (SEM) imaging was performed at the EPIC facility of the NUANCE Center at Northwestern University on a LEO Gemini 1525 microscope (InLens detector) operating at 2 kV, with a working distance of 2–4 mm for the side view examination, and a working distance of 6 mm for the top-down examination.

**X-ray Photoelectron Spectroscopy.** X-ray photoelectron spectroscopy (XPS) was performed at the Keck-II Center at Northwestern University on a Thermo Scientific ESCALAB 250Xi. A monochromatic Al K $\alpha$  (1486.74 eV) X-ray source was used with a 400  $\mu\text{m}$  spot size.

**DFT Calculations.** Electronic structure calculations presented in this work have been performed with the Amsterdam density functional (ADF) computational chemistry package.<sup>44</sup> Full geometry optimization, frequency, and polarizability calculations for surface bound monomer (both mono- and bidentate) and dimer TMA and DMACl complexes were completed using the Becke-Perdew (BP86) generalized gradient approximation (GGA) exchange correlation functional and a triple- $\zeta$  polarized (TZP) Slater orbital basis set.

Static Raman polarizabilities ( $\omega = 0$ ) were calculated in the RESPONSE package by two-point numerical differentiation using the RAMANRANGE keyword. Raman scattering intensities were determined by the scattering factor ( $S_j$ ):  $45\bar{\alpha}_j^2 + 7\bar{\gamma}_j^2$ , where  $\bar{\alpha}_j$  and  $\bar{\gamma}_j$  are the isotropic and anisotropic polarizability tensors with respect to the  $j$ th vibrational mode as shown in eq 1.

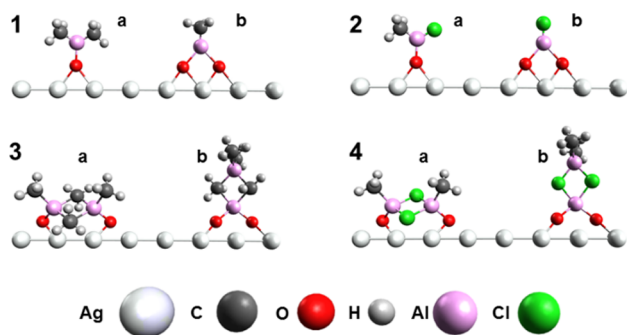
$$\frac{\partial\sigma}{\partial\Omega} = \frac{\pi^2}{\varepsilon_0^2} (\omega - \omega_j)^4 \frac{h}{8\pi c \omega_j} (S_j) \frac{1}{45 \left( 1 - \exp\left(-\frac{hc\omega_j}{k_B T}\right) \right)} \quad (1)$$

The lineshapes were simulated using eq 1 at 532 nm excitation and 298 K with a Lorentzian broadening full-width at half-maximum (fwhm) of 20  $\text{cm}^{-1}$  for comparison to experimental data.

## RESULTS AND DISCUSSION

If the monomer species is present on the surface after dosing TMA, then there will likely be either two (Scheme 1, 1a) or one (Scheme 1, 1b) methyl group(s) coordinated to the aluminum center. If the monomer species is present after dosing DMACl, then only one methyl group is likely associated with the monodentate (Scheme 1, 2a) species, since at least one ligand must be displaced during the ligand exchange

### Scheme 1. Representative Surface Reactions of TMA (1 and 3) and DMACl (2 and 4) on a Silver Oxide Surface, Resulting in Different Monomer (1 and 2) and Dimer (3 and 4) Surface Species<sup>a</sup>



<sup>a</sup>The monomer species are either monodentate (1a and 2a) or bidentate (1b and 2b) according to the aluminum atom surface coordination, whereas the dimer species are either parallel (3a and 4a) or perpendicular (3b and 4b) according to the orientation of the Al-bridge-Al-bridge plane with respect to the surface.

reaction, and a previous study has shown the methyl ligand to be slightly more reactive than the chlorine ligand.<sup>45</sup> This would leave only the chlorine group left in the bidentate (Scheme 1, 2b) case. Furthermore, we would reasonably expect a mixture of both monodentate and bidentate species, if monomers are present in either deposition. As a result, one would expect certain methyl group spectroscopic signatures in the TMA case, and some similar methyl group signatures in the DMACl monodentate case, as well as Al–Cl vibration(s) in both DMACl monomer cases. If the dimer species is present on the surface, then there should be unique vibrations associated with the bridging groups for each respective precursor (Scheme 1, 3a, 3b for TMA and Scheme 1, 4a, 4b for DMACl), regardless of whether the bridging groups are parallel or perpendicular to the silver surface. The vibrational modes associated with the bridging groups should be distinctly different than terminal groups. Furthermore, vibrations associated with the terminal methyl groups would likely be present in both cases.

In the lower wavenumber region (300–1300  $\text{cm}^{-1}$ ), the SER spectra show four and three clearly distinguishable peaks for TMA and DMACl, respectively (Figure 1). Three of the peaks

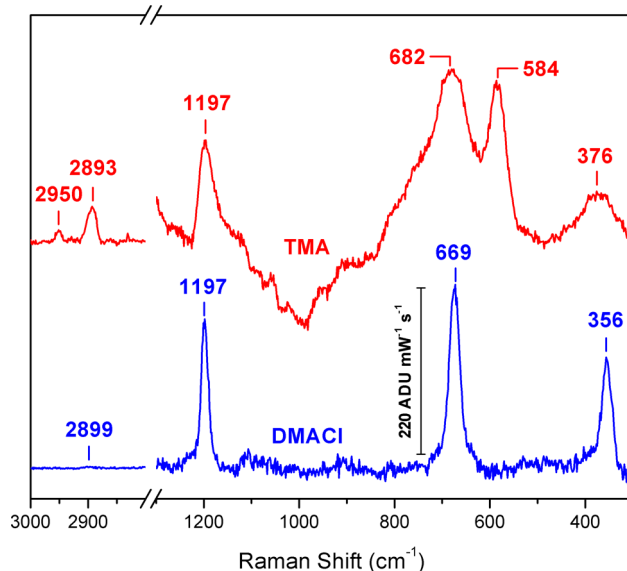


**Figure 1.** SER difference spectra of AgFON exposed to 60 s of TMA (1st cycle; red) and 60 s of DMACl (1st cycle; blue) in the low wavenumber (1300–300  $\text{cm}^{-1}$ ) and C–H (3000–2800  $\text{cm}^{-1}$ ) stretching regions. Data are shifted vertically for clarity.

are common between the two precursors: one at 1197  $\text{cm}^{-1}$  (symm.  $\nu(\text{Al}-\text{C})$ ,  $\delta(\text{CH}_3)$ ), one at 682/669  $\text{cm}^{-1}$  ( $\nu(\text{C}-\text{H})_{\text{rocking}}$ ), and another at 376/356  $\text{cm}^{-1}$  (symm.  $\nu(\text{Al-bridge})/\delta(\text{Al-bridge})$ ).<sup>46</sup> The peaks seen at 1197 and 682/669  $\text{cm}^{-1}$  are present in every simulated spectrum (Figures 2 and 3) of the possible alumina surface species with a coordinated methyl group (Scheme 1, 1a, 1b, 2a, 3a, 3b, 4a, and 4b) within error of the peaks seen experimentally. The only unique peak is seen in TMA at 584  $\text{cm}^{-1}$  ( $\nu(\text{bridged C-H rocking})$ ), which at first appears to line up with a terminal asymmetric Al–C stretching vibration in the simulated parallel dimer species at 591  $\text{cm}^{-1}$ . This vibrational mode, however, is more likely the bridged methyl rocking seen in theory at 551 and 576  $\text{cm}^{-1}$  in the parallel and perpendicular dimer models, respectively. One reason to suggest this unique peak is associated with the bridging methyl group (rather than the terminal methyl group)

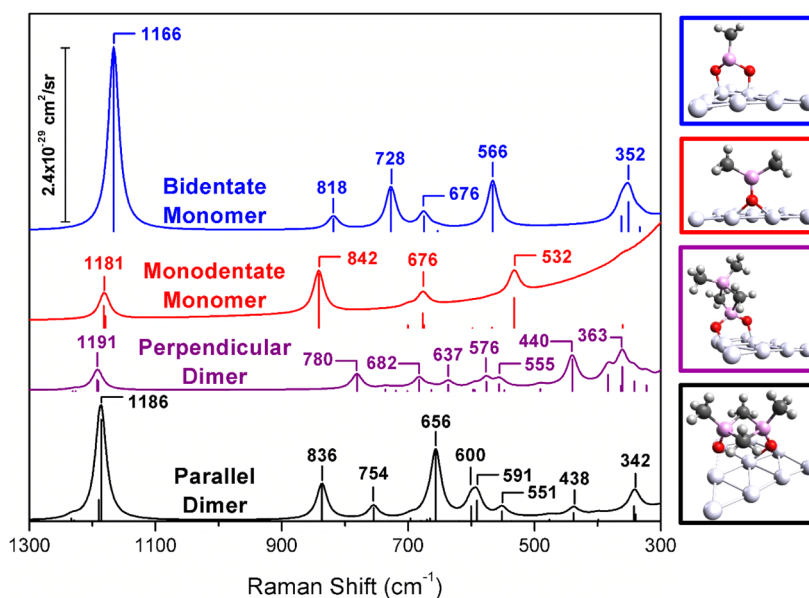


**Figure 2.** DFT-calculated Raman spectra (at 298 K) in the low wavenumber region (1300–300  $\text{cm}^{-1}$ ) of TMA surface species (parallel dimer (black), perpendicular dimer (purple), monodentate (red), and bidentate (blue)), with corresponding molecular structures.

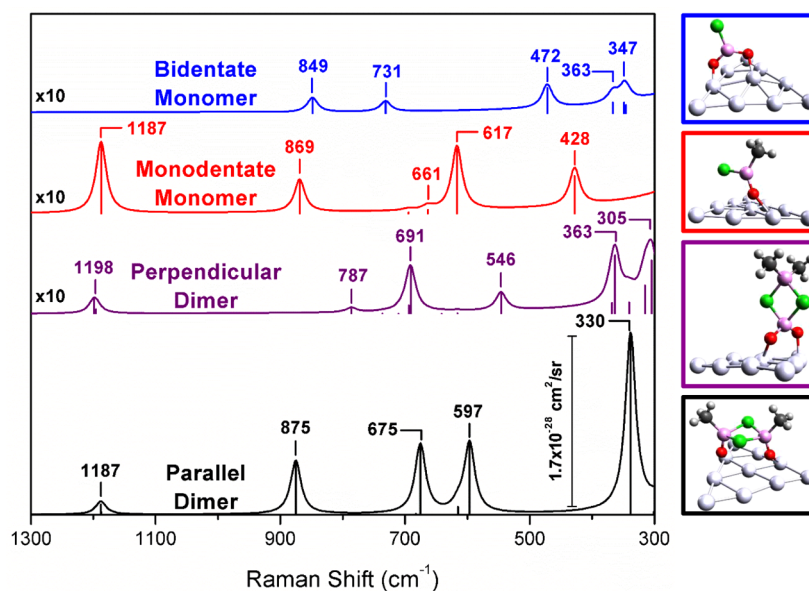


**Figure 3.** DFT-calculated Raman spectra (at 298 K) in the low wavenumber region (1300–300  $\text{cm}^{-1}$ ) of DMACl surface species (parallel dimer (black), perpendicular dimer (purple), monodentate (red), and bidentate (blue)), with corresponding molecular structures. The perpendicular dimer, monodentate, and bidentate spectra are magnified ( $\times 10$ ) for clarity of comparison.

is that the analogous terminal methyl stretch for DMACl is not observed in the experimental results. Figure 2 shows that this peak is weaker in the perpendicular configuration compared to parallel, but appears to be overestimated by DFT, as will be discussed further below. If the methyl stretch in question was a result of the monomer surface species, then one would expect to see two methyl stretches from the two possible monomer species, since the two symmetric Al–C stretches seen in the monodentate and bidentate TMA species are separated by a Raman shift of 34  $\text{cm}^{-1}$  according to theory. Furthermore, the predicted monomer Al–C stretches deviate significantly from experiment. For example, the monodentate species is predicted to be lower than the Al–C stretch observed by a margin of 51  $\text{cm}^{-1}$ .

The TMA peak at 376  $\text{cm}^{-1}$  only matches up with a bridging symmetric Al–C bend seen at 342 and 363  $\text{cm}^{-1}$  according to the parallel and perpendicular dimer models, respectively. Oddly enough, the corresponding bridging symmetric Al–C stretch, predicted to be at 438 and 440  $\text{cm}^{-1}$ , is not seen at all. The predicted symmetric mode may see differences in relative surface enhancement, however, thus making the symmetric mode difficult to observe. Neither monomer species contains Raman modes in the theoretical spectra that can be assigned to the experimentally observed 376  $\text{cm}^{-1}$  mode. The monodentate species has no significant Raman active vibrational modes below 500  $\text{cm}^{-1}$ . The bidentate species has only one predicted Raman active mode at 352  $\text{cm}^{-1}$  that is not assigned to the experimentally observed 376  $\text{cm}^{-1}$  mode, as the predicted

mode at  $352\text{ cm}^{-1}$  is an Al–O stretch. The  $376\text{ cm}^{-1}$  peak is not expected to result from an Al–O vibration, as all other Al–O vibrational modes are not observed. The Al–O vibrational modes are also not expected to be observable due to the alumina film being highly amorphous in nature.<sup>23,47</sup>

The simulated Raman spectra of the possible surface species of DMAcI (Figure 3) show four distinct locations of the Al–Cl stretch ( $472\text{ cm}^{-1}$  for the bidentate,  $428\text{ cm}^{-1}$  for the monodentate,  $305\text{ cm}^{-1}$  for the perpendicular dimer, and  $330\text{ cm}^{-1}$  for the parallel dimer). If the two monomer species were present in the DMAcI case, then two Al–Cl stretching peaks should be observed in the SER spectra, likely around the  $400\text{ cm}^{-1}$  region. Only one peak is observed in the region where the Al–Cl stretch is expected to occur, however, and this peak (at  $356\text{ cm}^{-1}$ ) matches up well with either the  $330$  or  $305\text{ cm}^{-1}$  peaks for the simulated dimer species. In comparison, the difference between the simulated Al–Cl stretch for the bidentate and experimental Al–Cl stretch is quite large ( $116\text{ cm}^{-1}$ ), suggesting the peak observed is not from the bidentate species. Likewise, the difference between the monodentate and experimental Al–Cl stretch ( $72\text{ cm}^{-1}$ ) suggests no monodentate species is observed either.

Thus, we assign the experimental vibrational spectra of both DMAcI and TMA to dimer species by a conclusive analysis in the  $300\text{--}1300\text{ cm}^{-1}$  region. For DMAcI:

1. The  $1197\text{ cm}^{-1}$  peak seen in SERS rules out the bidentate DMAcI species leaving the monodentate or dimer species as a possibility.
2. The absence of an Al–C stretching mode at either  $597$  or  $617\text{ cm}^{-1}$  (predicted for dimer [asymmetric] and monodentate [symmetric] species, respectively) experimentally suggests that the stretching mode is not enhanced, and hence not observed. The observation of this mode in theory is likely due to an overestimation of the Raman activity.
3. The presence of the  $356\text{ cm}^{-1}$  mode experimentally rules out the monodentate species as the theory predicts a bridging chloride mode for the dimers at  $330$  and  $305\text{ cm}^{-1}$ , much closer than the nearest monodentate vibration at  $428\text{ cm}^{-1}$ .

For TMA, the  $300\text{--}1300\text{ cm}^{-1}$  region has an even simpler analysis:

1. The presence of  $682$  and  $1197\text{ cm}^{-1}$  modes does not rule out the bidentate, monodentate, or dimer species as all models show these modes being Raman active.
2. Assuming a lack of enhancement of the asymmetric methyl stretching mode rules out the  $591\text{ cm}^{-1}$  observed in the theory spectrum. Thus, the  $584\text{ cm}^{-1}$  mode seen experimentally can be assigned to either a bridging methyl rocking mode for the dimers, predicted at  $551$  and  $576\text{ cm}^{-1}$ , or a symmetric methyl stretch in either the monodentate or bidentate species (predicted at  $532$  and  $566\text{ cm}^{-1}$ , respectively).
3. The presence of the  $376\text{ cm}^{-1}$  mode experimentally rules out the monodentate and bidentate species as only the dimers are predicted to have a Raman active vibration ( $342$  and  $363\text{ cm}^{-1}$ ) in the spectral region.

Ultimately there are few distinguishing features between the parallel dimer and perpendicular dimer models to help conclusively prove which species is being examined experimentally. The perpendicular dimer models do show a weak vibrational mode for TMA and DMAcI at  $555$  and  $546\text{ cm}^{-1}$ ,

respectively, that is not seen experimentally. This symmetric Al–C stretch, however, is not seen in the normal Raman spectra (see Figure S3) and may not appear in SERS due to an overestimation of Raman activity from the simple cluster model used. Vibrational modes that involve large changes in the perpendicular polarizability (with respect to the surface) are expected to be the more strongly enhanced on account of the electromagnetic field being strongest perpendicular to the surface,<sup>37</sup> which would then suggest the perpendicular dimer structure being more likely observed.

The C–H stretching region for each precursor is remarkably different; three distinguishable peaks are observed within the first cycle for TMA, whereas only one is barely noticeable for the DMAcI. The first TMA dose shows peaks at  $2831$ ,  $2893$ , and  $2950\text{ cm}^{-1}$ , with  $2893$  being the only distinguishable stretch beyond a few ALD cycles. Dosing DMAcI only yields one very weak peak at  $2899\text{ cm}^{-1}$ . The normal Raman spectra of TMA and DMAcI in the C–H region both show the same three peaks as in the SER spectrum of TMA (see Figure S3). The vibrational modes for DMAcI are noticeably weaker, with the mode at  $2827\text{ cm}^{-1}$  expected to be due to TMA dimer impurities.

It is unclear why the SER spectrum for DMAcI would be significantly weaker than its TMA counterpart, given that the peak at  $2895\text{ cm}^{-1}$  in the DMAcI liquid Raman spectrum is roughly 40% of the intensity of the corresponding TMA peak. All vibrational modes discussed in the SER spectra are summarized in Table S1. The normal Raman spectra of liquid TMA and DMAcI show common peaks to their SER spectra equivalents in the lower wavenumber region as well (see Figure S3). TMA shows two peaks at  $1201$  and  $684\text{ cm}^{-1}$  similar to the peaks found for the corresponding surface species at  $1197$  and  $682\text{ cm}^{-1}$ . Two additional peaks at  $496$  and  $452\text{ cm}^{-1}$  are only seen in the normal Raman spectrum of TMA, which is likely due to either ligand dissociation upon chemisorption onto the AgFON (preventing the vibration from occurring) or relative intensity changes by surface enhancement (as discussed with the Al-bridge symmetric stretch predicted at  $438\text{ cm}^{-1}$ ) DMAcI also shows common peaks to the SERS counterpart at  $1197$ ,  $709$ , and  $321\text{ cm}^{-1}$ . An additional peak not found on the SER spectrum of DMAcI is seen at  $580\text{ cm}^{-1}$  ( $\nu(\text{Al–C})_{\text{symm.}}$ ) in the normal Raman spectrum of DMAcI. It should be noted that the normal Raman spectra of these precursors in the liquid phase are of the dimer forms.

The experimental evidence thus far suggests dimer species are present on the heterogeneous silver surface, although monomer species are also likely present since they are thermodynamically more favorable.<sup>48</sup> However, we have both experimental and theoretical evidence that only the dimer species is observed. The lack of vibrational modes exclusive to the monomer species is likely a result of either the relative population of the dimer species, the relatively larger Raman scattering cross-section, or both. In the case of TMA, a larger Raman scattering cross-section for the dimer species is likely a result of a greater polarizability for the 3-center 2-electron bond in the bridging methyl group.<sup>49,50</sup> Also, the experimental SER spectra also show the surface species vibrations to be relatively the same in intensity between the two precursors, which is in contrast to what is seen between the possible monomer species for TMA and DMAcI. Figures 2 and 3 show the difference in scattering between the monodentate and bidentate species for TMA and DMAcI to be on the order of 10. In efforts to further substantiate the claim that dimer surface species are present,

QMS measurements were performed to evaluate changes in methane evolution from a silver surface as a function of number of ALD cycles. QCM, XPS, SEM, and LSPR measurements were also made to ensure no alternative processes were occurring that would result in different surface species between the two depositions.

Dimethylaluminum chloride as a precursor for alumina ALD behaves in a very similar fashion to trimethylaluminum; the most notable differences are the reactivity of the respective ligands (chloride vs methyl) and the byproduct (HCl gas and methane vs solely methane). Otherwise, the surface-gas chemistry is essentially the same as a means of growing films on substrates.<sup>45</sup> Our QCM (see Figure S4) and QMS (see Figures S5–S7) data support this notion, as the growth rate for both alumina precursors stabilizes at 1.1 Å per cycle. The alumina growth rate on silver using DMACl shows a larger initial mass gain during the first few cycles, however, and this is likely a consequence of chlorine adsorption. XPS spectra of DMACl-grown alumina on the AgFON (see Figures S8–S9) show visible chlorine peaks. The larger relative mass gain is unlikely to affect the surface species that this study is investigating during the alumina growth, as the chloride ligand is only expected to dissociate from DMACl after the water dose (this can be seen as HCl evolution in the QMS measurements in Figure S7). When QCM is performed during alumina ALD in a chamber that has been pretreated with 200 cycles of Ag ALD (thus simulating a silver surface analogous to the AgFON substrate), a change in the relative amount of methane evolved during the TMA and water doses can be seen when compared to a chamber pretreated with 30 cycles of alumina ALD (Figure 4a,b).

During the first several ALD cycles, the amount of methane evolved from the TMA dose is lower than what is seen during the TMA dose in later cycles, resulting in a methane ratio of about 1 between the two precursor doses. The methane ratio changes in later cycles before eventually stabilizing at about 1.6, the ratio seen in typical alumina ALD. This suggests the surface species present after the TMA dose has more methyl ligands associated with it when on a silver surface (such as would occur with an intact dimer species) than on a typical alumina surface (typically monomer species).<sup>46</sup> A similar phenomenon is seen when comparing the methane ratio of DMACl-utilized ALD on alumina and silver. On alumina, a stable ratio of 0.82 is seen with DMACl throughout multiple cycles. When the ALD is performed on silver, a methane ratio well below 0.82 is initially seen, before reaching the expected value after several cycles. Unlike TMA however, the methane ratio for DMACl continues to increase after 15 cycles. At present, it is not known why the methane ratio increases past the expected value for growing on an alumina surface. SEM micrographs (see Figures S10–S11) show surface reconstruction occurring as a result of HCl exposure, however this is unlikely to affect the ratio of methane evolution, especially in later cycles when surface reconstruction has already occurred. It seems apparent, however, that chlorine being present on a silver surface has an impact on which monomer surface species is most stable. In the case of later cycles, a higher methane ratio would suggest more bidentate monomer structures (Scheme 1, 2b). Nonetheless, the QMS measurements from both precursors support the previous SER spectra assignments of dimeric methylalumina species (and thus bridging moieties) being present on the AgFON surface during the initial ALD cycles.

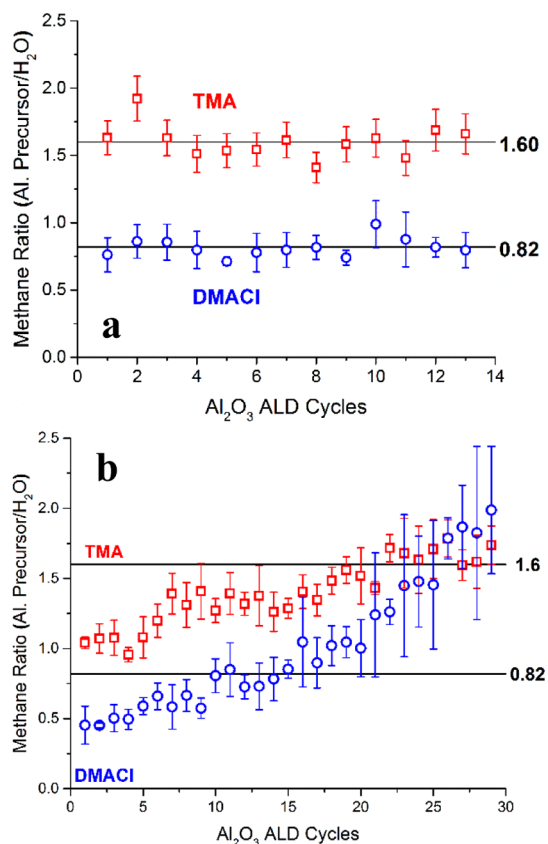


**Figure 4.** Ratio of methane evolved during precursor doses as a function of ALD cycle from alumina ALD at 70 °C on (a) alumina and (b) silver surfaces using both TMA (red) and DMACl (blue). Methane measurements were made using QMS in triplicate. The horizontal lines at methane ratios of 1.6 and 0.82 indicate the average methane ratios from alumina ALD on an alumina surface using TMA and DMACl, respectively. On a silver surface, the methane ratio for both alumina precursors clearly increases toward the alumina surface ratios as the number of ALD cycles increases.

The XPS spectrum of TMA-grown alumina on a AgFON shows a shift in the relative contribution from two constituent peaks in the O 1s signal as the number of ALD cycles increases (see Figure S9). Two constituent peaks are resolved in the O 1s signal for all samples; 1 cycle TMA (1cTMA) shows peaks at 531.9(2.4) and 530.2(1.6) eV, 10cTMA shows peaks at 532.0(2.2) and 530.6(1.4) eV, and 100cTMA shows peaks at 532.1(2.6) and 530.9(2.8) eV. The first constituent peak centered at 532 eV does not change in binding energy (BE) or fwhm, while decreasing in relative intensity from 1 to 100 ALD cycles. This peak is attributed to OH<sup>-</sup>, which has been found on aluminum oxide (made via various treatments) at 532.4 eV,<sup>51</sup> thus indicating there are hydroxyl-like nucleation sites on the AgFON for the alumina to grow. These nucleation sites are regenerated during the ALD process only on the surface (as expected), resulting in a decrease in relative contribution to the oxygen signal compared to the other constituent peak. The second constituent peak gradually shifts by +0.7 eV while increasing in relative intensity and broadening by 1.2 eV fwhm as the number of ALD cycles increases, and has been associated with O<sup>2-</sup> on aluminum oxide at 531.0 eV. The characteristics of this constituent peak suggests there is very little O<sup>2-</sup>-type oxide on the AgFON before alumina ALD, and that the oxide grows in after several ALD cycles. It should be noted that the XPS

characterization was done *ex-situ* and consequently the surface may have been altered during air transfer.

It is also important to point out that two constituent peaks show up in the Cl 2p signal for 1 and 10 cycles of DMACl-grown alumina on AgFON (see Figure S8), before growing into one discernible peak at 100 ALD cycles. These two components may be associated with adsorbed and ionic chlorine constituents on silver<sup>52</sup> and alumina, respectively. This would explain why only 1 peak is seen at 100 cycles, as the penetration depth of XPS for a metal oxide is less than the 11 nm of alumina deposited, resulting in no adsorbed chlorine on silver being probed.

The evolution of HCl gas in the DMACl ALD appears to chemically anneal the rough features of the AgFON substrate, resulting in a shift in the LSPR and a decrease in Raman enhancement (see SEM micrographs and *operando* LSPR spectra in Figures S10–S13), and while this does not appear to affect the growth of the alumina film, it does affect SERS. For the first full cycle, however, we can compare which vibrations are common and which are uniquely present for DMACl and for TMA. Since the HCl gas produced during DMACl ALD does not evolve until the water dose, the enhancement factor of the AgFON is not affected during the TMA/DMACl half-cycle that is analyzed within this paper. Unfortunately this does prevent the use of DMACl to measure SERS signal as a function of ALD cycle (and thus distance from the surface) like what was previously done with TMA.<sup>30</sup>

## CONCLUSIONS

The work described herein shows how *operando* SERS is effective in identifying new surface species that other methods fail to reveal. The SER spectra presented show vibrational modes associated with bridging moieties are present for methylalumina surface species resulting from dosing TMA and DMACl on a SERS-active substrate. These bridging moieties are indicative of dimer-type structures, likely in a perpendicular orientation, that persists throughout the course of the experiment. Stable dimer surface species have not previously been identified using other methods. Furthermore, predicted vibrational modes for monomer species (which are thermodynamically more favorable and thus also expected during the ALD process) were not observed. For the first time, *operando* LSPR measurements were also performed during ALD to show that the HCl gas evolved during DMACl-mediated alumina ALD compromises the structure of the SERS-active substrate. Ultimately this study shows how *operando* SERS can be applied toward acquiring unique structural information about surface species during a deposition by comparing precursors. *Operando* SERS is highly sensitive and can be applied in other surface-sensitive studies that benefit from probing the low wavenumber vibrational, such as catalytic reactions that involve metal–oxygen or metal–carbon bond formation.

## ASSOCIATED CONTENT

### Supporting Information

The Supporting Information is available free of charge on the ACS Publications website at DOI: 10.1021/jacs.6b12709.

Raman spectra of precursors, QCM measurements of depositions, X-ray photoelectron spectra of AgFON with varying alumina thicknesses, SEM micrographs of

AgFON, *operando* LSPR spectra during depositions, and QMS measurements of depositions. (PDF)

## AUTHOR INFORMATION

### Corresponding Author

\*E-mail: vanduyne@northwestern.edu

### ORCID

Ryan A. Hackler: 0000-0003-4698-6074

Michael O. McAnally: 0000-0002-8681-2952

Richard P. Van Duyne: 0000-0001-8861-2228

### Notes

The authors declare no competing financial interest.

## ACKNOWLEDGMENTS

The authors gratefully acknowledge financial support from the Northwestern University Institute for Catalysis in Energy Processes (ICEP). ICEP is funded through the U.S. Department of Energy, Office of Basic Energy Sciences (Award Number DE-FG02-03ER15457). M.O.M. acknowledges support from the National Science Foundation Graduate Fellowship Research Program under Grant No. DGE-0824162. This work made use of the EPIC facility (NUANCE Center-Northwestern University), which has received support from the MRSEC program (NSF DMR-1121262) at the Materials Research Center; the International Institute for Nanotechnology (IIN); and the State of Illinois, through the IIN.

## REFERENCES

- (1) George, S. M. *Chem. Rev.* **2010**, *110*, 111–131.
- (2) Puurunen, R. L. *J. Appl. Phys.* **2005**, *97*, 121301.
- (3) Miikkulainen, V.; Leskelä, M.; Ritala, M.; Puurunen, R. L. *J. Appl. Phys.* **2013**, *113*, 021301.
- (4) Suntola, T. *Thin Solid Films* **1992**, *216*, 84–89.
- (5) Leskelä, M.; Ritala, M. *Thin Solid Films* **2002**, *409*, 138–146.
- (6) Ferguson, J. D.; Smith, E. R.; Weimer, A. W.; George, S. M. *J. Electrochem. Soc.* **2004**, *151*, G528–G535.
- (7) Ritala, M.; Leskelä, A. In *Handbook of Thin Film Materials*; Nalwa, H. S., Ed.; Academic Press: San Diego, CA, 2001; Vol. 1, pp 103.
- (8) Peters, A. W.; Li, Z.; Farha, O. K.; Hupp, J. T. *ACS Nano* **2015**, *9*, 8484–8490.
- (9) Aaltonen, T.; Alen, P.; Ritala, M.; Leskelä, M. *Chem. Vap. Deposition* **2003**, *9*, 45–49.
- (10) Lu, J.; Stair, P. C. *Langmuir* **2010**, *26*, 16486–16495.
- (11) Lu, J.; Stair, P. C. *Angew. Chem., Int. Ed.* **2010**, *49*, 2547–2551.
- (12) Lu, J.; Fu, B.; Kung, M. C.; Xiao, G.; Elam, J. W.; Kung, H. H.; Stair, P. C. *Science* **2012**, *335*, 1205–1208.
- (13) Feng, H.; Libera, J. A.; Stair, P. C.; Miller, J. T.; Elam, J. W. *ACS Catal.* **2011**, *1*, 665–673.
- (14) Christensen, S. T.; Elam, J. W.; Rabuffetti, F. A.; Ma, Q.; Weigand, S. J.; Lee, B.; Seifert, S.; Stair, P. C.; Poepplmeier, K. R.; Hersam, M. C.; Bedzyk, M. J. *Small* **2009**, *5*, 750–757.
- (15) Baker, L.; Cavanagh, A. S.; Seghete, D.; George, S. M.; Mackus, A. J. M.; Kessels, W. M. M.; Liu, Z. Y.; Wagner, F. T. *J. Appl. Phys.* **2011**, *109*, 084333.
- (16) Li, J.; Liang, X.; King, D. M.; Jiang, Y.-B.; Weimer, A. W. *Appl. Catal., B* **2010**, *97*, 220–226.
- (17) Masango, S. S.; Peng, L.; Marks, L. D.; Van Duyne, R. P.; Stair, P. C. *J. Phys. Chem. C* **2014**, *118*, 17655–17661.
- (18) Biener, J.; Baumann, T. F.; Wang, Y.; Nelson, E. J.; Kucheyev, S. O.; Hamza, A. V.; Kemell, M.; Ritala, M.; Leskelä, M. *Nanotechnology* **2007**, *18*, 055303.
- (19) Christensen, S. T.; Feng, H.; Libera, J. A.; Guo, N.; Miller, J. T.; Stair, P. C.; Elam, J. W. *Nano Lett.* **2010**, *10*, 3047–3051.
- (20) Weber, M. J.; Mackus, A. J. M.; Verheijen, M. A.; Marel, C.; Kessels, W. M. M. *Chem. Mater.* **2012**, *24*, 2973–2977.

- (21) Lei, Y.; Liu, B.; Lu, J.; Lobo-Lapidus, R. J.; Wu, T.; Feng, H.; Xia, X.; Mane, A. U.; Libera, J. A.; Greeley, J.; Miller, J. T.; Elam, J. W. *Chem. Mater.* **2012**, *24*, 3525–3533.
- (22) Dasgupta, N. P.; Liu, C.; Andrews, S.; Prinz, F. B.; Yang, P. J. *Am. Chem. Soc.* **2013**, *135*, 12932–12935.
- (23) Miikkulainen, V.; Leskela, M.; Ritala, M.; Puurunen, R. L. *J. Appl. Phys.* **2013**, *113*, 021301.
- (24) Mondloch, J. E.; Bury, W.; Fairen-Jimenez, D.; Kwon, S.; DeMarco, E. J.; Weston, M. H.; Sarjeant, A. A.; Nguyen, S. T.; Stair, P. C.; Snurr, R. Q.; Farha, O. K.; Hupp, J. T. *J. Am. Chem. Soc.* **2013**, *135*, 10294–10297.
- (25) Du, Y.; George, S. M. *J. Phys. Chem. C* **2007**, *111*, 8509–8517.
- (26) Fu, Y.; Li, B.; Jiang, Y.-B.; Dunphy, D. R.; Tsai, A.; Tam, S.-Y.; Fan, H.; Zhang, H.; Rogers, D.; Rempe, S.; Atanassov, P.; Cecchi, J. L.; Brinker, C. J. *J. Am. Chem. Soc.* **2014**, *136*, 15821–15824.
- (27) Zaera, F. J. *Mater. Chem.* **2008**, *18*, 3521–3526.
- (28) Zaera, F. J. *Phys. Chem. Lett.* **2012**, *3*, 1301–1309.
- (29) Masango, S. S.; Hackler, R. A.; Henry, A.-I.; McAnally, M. O.; Schatz, G. C.; Stair, P. C.; Van Duyne, R. P. *J. Phys. Chem. C* **2016**, *120*, 3822–3833.
- (30) Masango, S. S.; Hackler, R. A.; Large, N.; Henry, A.-I.; McAnally, M. O.; Schatz, G. C.; Stair, P. C.; Van Duyne, R. P. *Nano Lett.* **2016**, *16*, 4251–4259.
- (31) Lu, J.; Liu, B.; Guisinger, N. P.; Stair, P. C.; Greeley, J. P.; Elam, J. W. *Chem. Mater.* **2014**, *26*, 6752–6761.
- (32) Dillon, A. C.; Ott, A. W.; Way, J. D.; George, S. M. *Surf. Sci.* **1995**, *322*, 230–242.
- (33) Goldstein, D. N.; McCormick, J. A.; George, S. M. *J. Phys. Chem. C* **2008**, *112*, 19530–19539.
- (34) Jeanmaire, D. L.; Van Duyne, R. P. *J. Electroanal. Chem. Interfacial Electrochem.* **1977**, *84*, 1–20.
- (35) Dieringer, J. A.; Lettan, R. B.; Scheidt, K. A.; Van Duyne, R. P. *J. Am. Chem. Soc.* **2007**, *129*, 16249–16256.
- (36) Stiles, P. L.; Dieringer, J. A.; Shah, N. C.; Van Duyne, R. P. *Annu. Rev. Anal. Chem.* **2008**, *1*, 601–626.
- (37) Schatz, G. C.; Van Duyne, R. P. Electromagnetic Mechanism of Surface-Enhanced Spectroscopy. In *Handbook of Vibrational Spectroscopy*; Chalmers, J. M., Griffiths, P. R., Eds.; Wiley: New York, 2002; pp 759–774.
- (38) Willets, K. A.; Van Duyne, R. P. *Annu. Rev. Phys. Chem.* **2007**, *58*, 267–297.
- (39) Stiles, P. L.; Dieringer, J. A.; Shah, N. C.; Van Duyne, R. P. *Annu. Rev. Anal. Chem.* **2008**, *1*, 601–626.
- (40) Lombardi, J. R.; Birke, R. L. *J. Phys. Chem. C* **2008**, *112*, 5605–5617.
- (41) Campion, A.; Ivanecky, J. E., III; Child, C. M.; Foster, M. J. *Am. Chem. Soc.* **1995**, *117*, 11807–11808.
- (42) Valley, N.; Greeneltch, N. G.; Van Duyne, R. P.; Schatz, G. C. *J. Phys. Chem. Lett.* **2013**, *4*, 2599–2604.
- (43) Greeneltch, N. G.; Blaber, M. G.; Henry, A.-I.; Schatz, G. C.; Van Duyne, R. P. *Anal. Chem.* **2013**, *85*, 2297–2303.
- (44) Baerends, E. J.; Ziegler, T.; Autschbach, J.; Bashford, D.; Bérces, A.; Bickelhaupt, F. M.; Bo, C.; Boerrigter, P. M.; Cavallo, L.; Chong, D. P.; Deng, L.; Dickson, R. M.; Ellis, D. E.; van Faassen, M.; Fan, L.; Fischer, T. H.; Fonseca Guerra, C.; Franchini, M.; Ghysels, A.; Giammona, A.; van Gisbergen, S. J. A.; Götz, A. W.; Groeneveld, J. A.; Gritsenko, O. V.; Grüning, M.; Gusarov, S.; Harris, S. E.; van den Hoek, P.; Jacob, C. R.; Jacobsen, H.; Jensen, L.; Kaminski, J. W.; van Kessel, G.; Kootstra, F.; Kovalenko, A.; Krykunov, M. V.; van Lenthe, E.; McCormack, D. A.; Michalak, A.; Mitoraj, M.; Morton, S. M.; Neugebauer, J.; Nicu, V. P.; Noodleman, L.; Osinga, V. P.; Patchkovskii, S.; Pavanello, M.; Philipsen, P. H. T.; Post, D.; Pye, C. C.; Ravenek, W.; Rodríguez, J. I.; Ros, P.; Schipper, P. R. T.; van Schoot, H.; Schreckenbach, G.; Seldenthuis, J. S.; Seth, M.; Snijders, J. G.; Solà, M.; Swart, M.; Swerhone, D.; te Velde, G.; Vernooijs, P.; Versluis, L.; Visscher, L.; Visser, O.; Wang, F.; Wesolowski, T. A.; van Wezenbeek, E. M.; Wiesenekker, G.; Wolff, S. K.; Woo, T. K.; Yakovlev, A. L. ADF2014, SCM, *Theoretical Chemistry*; Vrije Universiteit: Amsterdam, The Netherlands, <http://www.scm.com>.
- (45) Matero, R.; Rahtu, A.; Ritala, M. *Langmuir* **2005**, *21*, 3498–3502.
- (46) Yamamoto, O. *Bull. Chem. Soc. Jpn.* **1962**, *35*, 619–622.
- (47) Xiong, G.; Elam, J. W.; Feng, H.; Han, C. Y.; Wang, H.-H.; Iton, L. E.; Curtiss, L. A.; Pellin, M. J.; Kung, M.; Stair, P. C. *J. Phys. Chem. B* **2005**, *109*, 14059–14063.
- (48) Soto, C.; Wu, R.; Bennett, D. W.; Tysoe, W. T. *Chem. Mater.* **1994**, *6*, 1705–1711.
- (49) McGrady, G. S.; Turner, J. F. C.; Ibberson, R. M.; Prager, M. *Organometallics* **2000**, *19*, 4398–4401.
- (50) Stammer, H.-G.; Blomeyer, S.; Berger, R. J. F.; Mitzel, N. W. *Angew. Chem., Int. Ed.* **2015**, *54*, 13816–13820.
- (51) van den Brand, J.; Sloof, W. G.; Terryn, H.; de Wit, J. H. W. *Surf. Interface Anal.* **2004**, *36*, 81–88.
- (52) Kautek, W.; Gordon, G. G., II. *J. Electrochem. Soc.* **1990**, *137*, 3405–3409.